




**RESEARCH ARTICLE** OPEN ACCESS

# Molecular Design Strategies for High-Voltage Organic Cathodes

Sungil Hong<sup>1,2</sup>  | Alae Eddine Lakraychi<sup>1,3,4</sup> | Artur Lyssenko<sup>1,5,6</sup> | Abhishek Ashwin Panchal<sup>1,3,4</sup> | Harshan Reddy Gopidi<sup>1,3,4</sup> | Pieremanuele Canepa<sup>1,3,4</sup> | Rafael Gómez-Bombarelli<sup>1,5</sup>  | Yan Yao<sup>1,3,4</sup> | Rajeev Surendran Assary<sup>1,2</sup> 

<sup>1</sup>Energy Storage Research Alliance (ESRA), Argonne National Laboratory, Lemont, Illinois, USA | <sup>2</sup>Materials Science Division, Argonne National Laboratory, Lemont, Illinois, USA | <sup>3</sup>Department of Electrical and Computer Engineering, University of Houston, Houston, Texas, USA | <sup>4</sup>Texas Center for Superconductivity at the University of Houston (TcSUH), University of Houston, Houston, Texas, USA | <sup>5</sup>Department of Materials Science and Engineering, Massachusetts Institute of Technology, Cambridge, Massachusetts, USA | <sup>6</sup>Department of Chemistry and Chemical Biology, Harvard University, Cambridge, Massachusetts, USA

**Correspondence:** Yan Yao ([yyao4@central.uh.edu](mailto:yyao4@central.uh.edu)) | Rajeev Surendran Assary ([assary@anl.gov](mailto:assary@anl.gov))

**Received:** 4 December 2025 | **Revised:** 13 May 2026 | **Accepted:** 15 May 2026

**Keywords:** density functional theory | energy storage | molecular engineering | organic cathodes

## ABSTRACT

Organic electrode materials (OEMs) offer promising pathways toward sustainable and high-performance rechargeable batteries, yet their practical implementation is limited by rigid crystal structures, poor electronic conductivity, and low redox potential. Here, we conduct a systematic molecular-level investigation of two organic cathodes, phenazine-1,4,6,9-tetrone (PzTO) and dithiin-fused naphthazarin (5,8-dihydroxy-1,4-naphthoquinone) (DNP), through a combined computational and experimental approach. Solution-phase cyclic voltammetry reveals a substantial redox potential gap between them, with DNP exhibiting a reduction potential  $\sim 500$  mV higher than PzTO. This difference becomes more pronounced in solid state measurements, where the first reduction potentials reach  $\sim 3.68$  V vs.  $\text{Li}^+/\text{Li}$  for DNP and 3.08 V for PzTO. By dissecting the molecular origins of these trends, we identify two governing features: (i) changes of aromaticity upon reduction (differential aromaticity) and (ii) Li–O coordination number. Density functional theory calculations confirm that these features strongly modulate lithiation free energies. Extending our analysis to a series of hypothetical derivatives of PzTO and DNP, we establish a linear relationship between differential aromaticity and lithiation free energy and show that the introduction of additional Li–O coordination enhances redox potentials. Taken together, these molecular engineering insights offer a mechanistic foundation for rationalizing high-voltage performance and guiding the design of next-generation OEMs.

## 1 | Introduction

Organic electrode materials (OEMs) have attracted increasing attention as sustainable and potentially low-cost alternatives to conventional inorganic counterparts in energy storage [1–3]. To date, numerous organic molecules have been investigated,

exhibiting tunable physicochemical properties and promising material-level energy metrics [4–7]. Despite these advances, the practical implementation of OEMs remains challenged by rigid crystal structures, insufficient electronic conductivity, and lack of high redox potentials [8–11]. Among OEMs, carbonyl-based compounds are the most extensively studied, owing to

Sungil Hong and Alae Eddine Lakraychi contributed equally to this work.

This is an open access article under the terms of the [Creative Commons Attribution-NonCommercial](https://creativecommons.org/licenses/by-nc/4.0/) License, which permits use, distribution and reproduction in any medium, provided the original work is properly cited and is not used for commercial purposes.

© 2026 The Author(s). *Advanced Energy Materials* published by Wiley-VCH GmbH

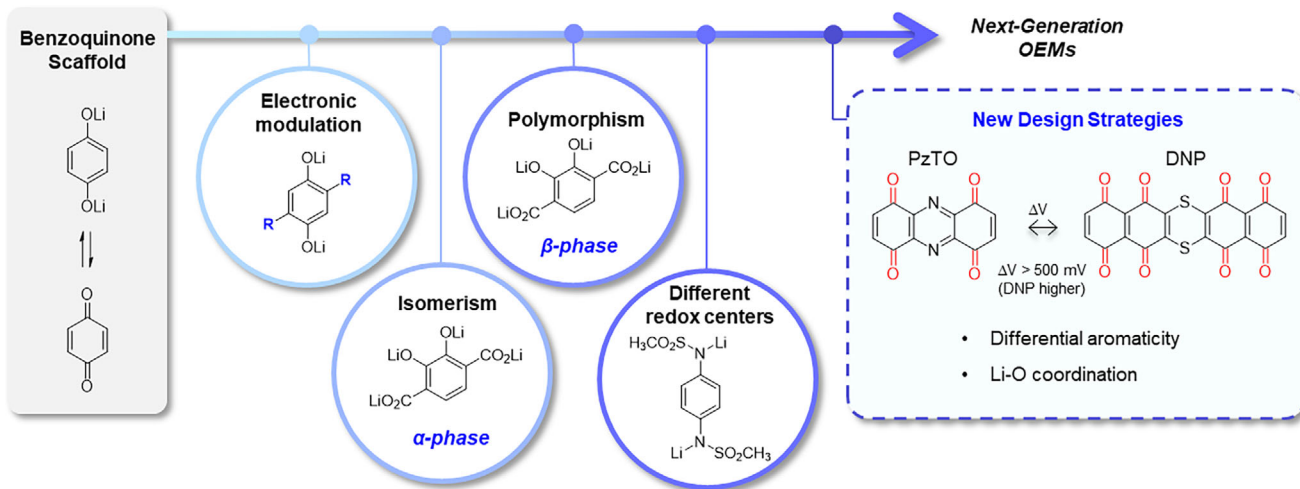


**FIGURE 1** | Design strategies for next-generation carbonyl-based organic electrode materials (OEMs). Previously suggested strategies are summarized in circles. A new design strategy is enabled by a comparative study of two OEMs, phenazine-1,4,6,9-tetrone (PzTO) and dithiin-fused naphthazarin (5,8-dihydroxy-1,4-naphthoquinone) (DNP), as depicted in the right block.

their potential to simultaneously deliver high energy and power densities while maintaining high cycling stability [4, 6]. Within this class of compounds, several OEMs have demonstrated notably high specific capacities approaching  $\sim 500 \text{ mAh g}^{-1}$ . Yet, their redox potentials remain confined to the low region of 2–3 V vs.  $\text{Li}^+/\text{Li}$ , where state-of-the-art inorganic cathodes operate at 3–4 V vs.  $\text{Li}^+/\text{Li}$  [12, 13]. To be competitive with inorganic systems, the redox potential must be increased by about 1 V [14].

Significant progress toward the high-voltage requirement has been made, with many research groups reporting organic cathodes operating at 3.0–3.5 V vs.  $\text{Li}^+/\text{Li}$ , which represents important steps toward narrowing the redox potential gap [15–22]. In Figure 1, the design strategies for improving redox potential of carbonyl-based OEMs are summarized, broadly categorized into four: (i) electronic modulation via functional group substitution [15, 23–29], (ii) inducing coulombic interactions through isomerism [30, 31], (iii) crystal structure tuning via polymorphism [32], and (iv) including novel functional groups with intrinsically elevated redox potentials [16, 33–35]. These approaches either involve increasing molecular weight, thereby limiting theoretical capacity, or remain unexplored on molecular scaffolds due to the complexity of synthesis and characterization.

In parallel, considerable computational efforts have also been devoted to discovering novel organic compounds with improved redox potentials [36–39]. These reports highlight candidates with extended aromatic systems [38, 40], various spatial arrangements and additional incorporation of carbonyl redox centers [36, 38, 39], and heteroatom doping such as nitrogen, oxygen, and sulfur, thereby extending the chemical library of newly discovered functional groups [38, 40, 41]. Despite these theoretical insights, most advances have either revisited the same design principles outlined above or proposed exotic molecular architectures that remain synthetically hard to realize [42–45]. This underscores the challenge of achieving breakthroughs toward the 4 V-class organic cathodes using purely theory-driven molecular strategies.

In this work, we address these gaps by conducting a systematic comparative study of reported organic cathode materials, combining experimental and computational approaches to identify chemical and structural descriptors that directly govern redox potentials. As shown in Figure 1, we focus on two high-voltage candidates whose underlying redox mechanisms have not been fully explained by existing design strategies: phenazine-1,4,6,9-tetrone (PzTO) [46] and dithiin-fused naphthazarin (5,8-dihydroxy-1,4-naphthoquinone) (DNP) [47, 48]. PzTO is an analog of pyrazine-fused bis-tetraaminobenzoquinone (TAQ), a material known for high electrical conductivity and high capacity [49–51]. Because the amino ( $\text{NH}_2$ ) groups of TAQ provide strong electron-donating character and reduce solubility, we selected the amino-free analog PzTO for the molecular study. The second molecule, DNP, has also been reported to exhibit unusually high operating potentials and good cycling stability [47, 48]. Here, we evaluated the electrochemistry of PzTO and DNP and performed computational chemistry calculations to reveal the origin of their redox potential difference. Guided by these insights, we further explored a series of hypothetical derivatives through computational screening, identifying two key descriptors: (1) aromaticity change upon reduction and (2) Li–O coordination number, that collectively enable substantial enhancement of redox potential. These structure-property relationships establish new molecular design principles for the development of synthetically accessible 4 V-class organic cathodes.

## 2 | Methods

### 2.1 | Experimental Details

#### 2.1.1 | General

The following chemicals and solvents were purchased from commercial suppliers and used without further purification: DNP-Li (CAS: 1882849-59-3) was purchased from TCI Chemical; 2,5-diethoxyaniline, 1,4-diethoxy-2-nitrobenzene, ammonium cerium (IV) nitrate (CAN), potassium tert-butoxide,

tetra-*n*-butylammonium perchlorate (TBAP), anhydrous tetrahydrofuran, chloroform, and ethanol from Sigma–Aldrich; anhydrous dimethylformamide and ferrocene from Alfa Aesar. Attenuated total reflectance–Fourier transform infrared (ATR–FTIR) spectra were recorded on a Thermo Scientific Nicolet iS5 spectrometer. Powder X-ray diffraction (PXRD) patterns were obtained using Rigaku MiniFlex 600 with Cu  $K\alpha$  radiation ( $\lambda = 1.5406 \text{ \AA}$ ) operating at 40 kV and 15 mA. The data were recorded in a  $2\theta$  range of  $5^\circ$ – $60^\circ$  with a step width of  $0.01^\circ$  and a scan rate of  $1.8^\circ \text{ min}^{-1}$ .

## 2.1.2 | Synthesis

PzTO was synthesized in two steps via the 1,4,6,9-Tetraethoxyphenazine (TEP) intermediate, following a previously reported procedure [46], as illustrated in Scheme S1.

**2.1.2.1 | TEP.** Inside an argon-filled glovebox, potassium tert-butoxide (1.18 g, 10.5 mmol) was added to a solution of 2,5-diethoxyaniline (1.5 g, 8.28 mmol) and 1,4-diethoxy-2-nitrobenzene (1.11 g, 5.3 mmol) in anhydrous tetrahydrofuran (10 mL) (3.2 g, 29 mmol). The resulting blackish mixture was stirred at room temperature for 2 h. The solution was then poured into deionized water (20 mL) to give a dark orange solution that was extracted with chloroform ( $3 \times 10 \text{ mL}$ ). The combined organic extracts were evaporated under reduced pressure to give an orange-brown solid. This crude product was dissolved in chloroform and purified using silica-gel chromatography using 100% chloroform as the eluent, yielding TEP as a dark orange solid (0.9 g, 50%).

ATR–FTIR  $\bar{\nu}$  ( $\text{cm}^{-1}$ ) = 3594, 3555, 3073, 2986, 2969, 2932, 2875, 1652, 1620, 1497, 1474, 1395, 1373, 1316, 1262, 1240, 1217, 1153, 1116, 1032, 899, 837, 810, 760, 661 (Figure S1 shows the FTIR spectrum).

**2.1.2.2 | PzTO.** A suspension of TEP (356 mg, 1.00 mmol) in acetonitrile (25 mL) was treated with an aqueous solution of CAN (3.58 g, 6.52 mmol) in 10% nitric acid (5 mL). The mixture rapidly turned into a dark solution and progressively yielded a yellowish-brown precipitate. The reaction mixture was stirred for 3 h at room temperature, after which 10% nitric acid (20 mL) was added. The resulting solid was filtered and thoroughly washed with ethanol (10 mL) and dried to afford PzTO as a yellowish-brown solid (100 mg, 42%).

ATR–FTIR  $\bar{\nu}$  ( $\text{cm}^{-1}$ ) = 3352, 3330, 3061, 2991, 2947, 1699, 1674, 1662, 1593, 1450, 1358, 1249, 1203, 1086, 1039, 1002, 849, 745, 679 (see Figure S1)

The PXRD pattern of PzTO shown in Figure S2 matches that reported by Yao et al. [46], further confirming the formation of the desired compound.

## 2.1.3 | Electrochemistry

Cyclic voltammetry (CV) was performed inside an MBRAUN argon-filled glovebox (<0.5 ppm water and oxygen content) with a BioLogic VMP3 potentiostat (BioLogic Science Instrument). A

three-electrode cell setup with a glassy carbon working electrode (3 mm diameter, CH instruments), platinum wire counter electrode (CH instruments), a silver wire pseudo-reference electrode, and an electrolyte consisting of 0.1 M tetra-*n*-butylammonium perchlorate in anhydrous dimethylformamide, was used for measurements. Typically, 1 m of active material was dissolved in the electrolyte solution. The voltammograms were recorded in a glovebox at room temperature and scan rates ranging from 10 to  $400 \text{ mV s}^{-1}$ . Ferrocene was added to the solution after testing and used as an internal reference.

All experiments were performed at room temperature, and all cells were assembled inside the glovebox. Electrochemical measurements were recorded on a BioLogic VMP3 potentiostat. Active material, carbon black (super P), and polytetrafluoroethylene (PTFE) binder were mixed in a 6:3:1 mass ratio in an agate mortar for 20 min with the aid of isopropanol. The resulting rubber-like composite was calendared, dried in air for 6 h, and then dried under vacuum at  $70^\circ\text{C}$  overnight. Afterward, the self-standing electrode was cut into discs of diameter 5/16 inch. The typical areal mass loading of these composite electrodes is about  $2 \text{ mg cm}^{-2}$ . Coin cells were assembled using lithium foil with a 3/8 inch diameter, a membrane separator (Celgard 2325, 9/16 inch) impregnated with 100  $\mu\text{L}$  of 1 M lithium hexafluorophosphate ( $\text{LiPF}_6$ ) ethylene carbonate (EC) and dimethyl carbonate (DMC) (1:1, v/v) (LP30) electrolyte, and the above-prepared electrodes as cathodes. The cells were cycled within different potential windows at a cycling rate of 0.1 C unless stated otherwise.

The electronic conductivity of DNP was measured using the direct current (DC) polarization method. Specifically, 80 mg of pristine DNP–Li powder was packed into a polyetheretherketone (PEEK) die and pressed at 3 tons for 2 min to form a dense pellet of 290  $\mu\text{m}$  thickness. To improve electrical contact, 8 mg of carbon was added to both faces of the pellet, and the assembly was further pressed at 2 tons for 2 min, resulting in a three-layer pellet. The pellet was then subjected to different voltages, and the resulting current response was recorded using a potentiostat (BioLogic SP-200). Resistance was determined by plotting applied voltage vs. steady-state current and fitting the data to a linear function. The electronic conductivity ( $\sigma_e$ ) was calculated using the relation  $\sigma_e = t / (R \cdot S)$ , where  $t$  is the pellet thickness of DNP–Li,  $R$  is the slope of the linear fit, and  $S$  is the contact area.

## 2.2 | Computational Details

Density functional theory (DFT) calculations were carried out using the Gaussian 16 software package [52] at the  $\omega\text{B97X-D}$  level of theory [53] coupled with the 6–31+G(d,p) Pople basis set [54, 55]. Solvation effects were considered by using the Conductor-like Polarizable Continuum Model [56, 57], with the solvent being dimethyl sulfoxide (dielectric constant,  $\epsilon = 46.8$ ) as implemented in Gaussian, because it shares the polar aprotic nature of EC/DMC (1:1, v/v) electrolyte and its dielectric constant is close to the mean of those of EC ( $\epsilon = 89.8$ ) and DMC ( $\epsilon = 3.1$ ). Vibrational frequency calculations were performed to confirm that the structures were local minima of the potential energy surfaces by the absence of any imaginary frequencies. Small imaginary frequencies ( $<30 \text{ cm}^{-1}$ ) were ignored. Gibbs free energies ( $G$ ) were calculated assuming  $25^\circ\text{C}$  and 1 atm.

Lithiation free energies were converted to reduction potentials using Equation (1):

$$E_n = \frac{G(n\text{Li}) - G((n-1)\text{Li})}{F} - E_{\text{ref}} \quad (1)$$

where  $E_n$  is the reduction potential corresponding to the addition of the  $n$ th Li atom,  $G(n\text{Li})$  is the Gibbs free energy of a molecule containing  $n$  Li atoms,  $F$  is the Faraday constant, and  $E_{\text{ref}}$  is a constant (1.24 V) [36] used to convert computed reduction potentials with respect to the  $\text{Li}^+/\text{Li}$  electrode. The specific charge capacity ( $Q$ ) was computed using Equation (2):

$$Q = nF/M \quad (2)$$

where  $n$  is the number of Li atoms and  $M$  is the molecular weight. The lithiation and delithiation processes were modeled for 0–4 Li atoms, with Li atom positions determined by comparing the free energies of PzTO and DNP molecules (Section S2 provides details of the free-energy comparison). Molecular aromaticity was quantified using the Harmonic Oscillator Measure of Aromaticity (HOMA) [58–60], which is based on the bond lengths of atoms comprising (hetero)cycles:

$$\text{HOMA} = 1 - \frac{1}{n} \alpha_{XY} \sum_i (r_{XY,i} - R_{XY}^{\text{ref}}) \quad (3)$$

where  $\alpha_{XY}$  and  $R_{XY}^{\text{ref}}$  are predefined parameters for a bond between atoms  $X$  and  $Y$ , and  $r_{XY,i}$  is the  $X$ – $Y$  bond distance in the given structure. The summation is performed over all coordinate bonds in the (hetero)cycles. Other moieties attached to the cyclic backbone structures, e.g., hydrogens and functional groups, are ignored during the HOMA determination. The HOMA value is maximized at 1, which corresponds to benzene, and 0.5 is typically used to categorize molecules as aromatic ( $>0.5$ ) vs. non-aromatic ( $<0.5$ ). We used the parameters  $\alpha_{XY}$  and  $R_{XY}^{\text{ref}}$  suggested by Frizzo and Martins [61]. Benchmark calculations ensured that the HOMA coupled with the chosen parameters is applicable to DFT-optimized molecular structures, as shown in Section S3.

### 3 | Results and Discussion

#### 3.1 | Electrochemistry of PzTO and DNP

PzTO and DNP (Figure 2a,b) are redox-active molecules that share common molecular fragments. PzTO comprises two quinonoid units separated by a pyrazine ring, which gives rise to a multi-electron redox system involving the reduction of four carbonyl groups within an intermediate potential window. In comparison, DNP consists of two adjacent quinonoid units fused to another pair of adjacent quinonoid units via a dithiin ring, resulting in a multi-electron redox system. This configuration enables the reversible reduction of four carbonyl groups within a high-potential window and an additional four within a low-potential window.

To investigate the intrinsic electrochemical properties of PzTO and DNP at the molecular level, solution-phase CV was conducted in 0.1 M TBAP in dimethylformamide. Tetrabutylammonium ( $\text{TBA}^+$ ) was chosen as a working cation owing to its

non-coordinating nature, thereby avoiding any specific binding with oxygen atoms. The fourth-cycle voltammograms are shown in Figure 2c,d, and representative CVs over multiple cycles and various scan rates are provided in Figure S5. PzTO displays two symmetrical and reversible redox processes within the range of  $-1.25$  to  $-0.45$  V vs.  $\text{Fc}^+/\text{Fc}$ , each accounting for two-electron transfer, consistent with the reversible reduction of four carbonyl groups (Figure 2c). In comparison, DNP exhibits four sequential and reversible redox waves within the potential window of  $-2.00$  to  $0.80$  V vs.  $\text{Fc}^+/\text{Fc}$ , each involving a two-electron redox process, corresponding to the reduction and oxidation of eight carbonyl groups per molecule (Figure 2d). Notably, the electrochemical response of PzTO remains stable across four successive cycles (Figure S5b), whereas DNP displays pronounced changes characterized by notable peak shifts between the first and subsequent cycles (Figure S5e). This discrepancy is likely due to the different ion types involved: strongly coordinated  $\text{Li}^+$  ions are extracted from pristine DNP-Li in the initial cycle, whereas weakly coordinated  $\text{TBA}^+$  ions are involved in the subsequent cycles.

Table S1 summarizes the details of the half-wave potential ( $E_{1/2}$ ) and peak potential separation ( $\Delta E_p$ ) obtained from the fourth CV cycle. The fourth cycle was deliberately selected to ensure that only  $\text{TBA}^+$  participates in the ion exchange process, thereby eliminating any influence of  $\text{Li}^+$  on the redox potential. At a scan rate of  $100 \text{ mV s}^{-1}$ , PzTO exhibits  $\Delta E_p$  values in the range of 58–135 mV, indicative of high-to-moderate electrochemical reversibility. In contrast, DNP displays significantly larger  $\Delta E_p$  values (214–438 mV), characteristic of electrochemical irreversibility. This disparity likely arises from differences in intramolecular electronic delocalization, which is enhanced in PzTO owing to the acceptor-donor conjugation between quinone and pyrazine [62], but weakened in DNP because the dithiin ring acts as a non-conjugating linker between quinone units [63]. The first two redox events of DNP are positively shifted by approximately 500 mV relative to those of PzTO. Specifically, the  $E_{1/2}$  values (V vs.  $\text{Fc}^+/\text{Fc}$ ) of PzTO at  $-0.62$  and  $-0.93$  are shifted to  $+0.25$  and  $-0.11$  in DNP, respectively. To the best of our knowledge, such a substantial molecular-level increase in redox potential is unprecedented and warrants further investigation into its underlying origins.

To investigate the influence of  $\text{Li}^+$  coordination on the redox potential, PzTO and DNP electrodes were fabricated and assembled into coin cells for solid-state electrochemical measurements. The first discharge profiles are shown in Figure 2e, and the corresponding charge/discharge profiles for the first two cycles are provided in Figure S6. The discharge profile of PzTO features an initial pseudo-plateau followed by a sloping plateau within the potential range of 1.5–3.5 V vs.  $\text{Li}^+/\text{Li}$ . Both plateaus contribute nearly equally to the overall capacity, yielding a specific discharge capacity of  $350 \text{ mAh g}^{-1}$ , corresponding to 78% of the theoretical value. A pronounced capacity decay was observed in the subsequent cycle, attributed to substantial dissolution of the active material into the electrolyte, as visually confirmed by the clear brownish coloration of the PzTO solution (Figure S7).

In contrast, DNP displays two pseudo-plateaus in a higher-potential region (2.8–4.0 V vs.  $\text{Li}^+/\text{Li}$ ). Both plateaus contribute

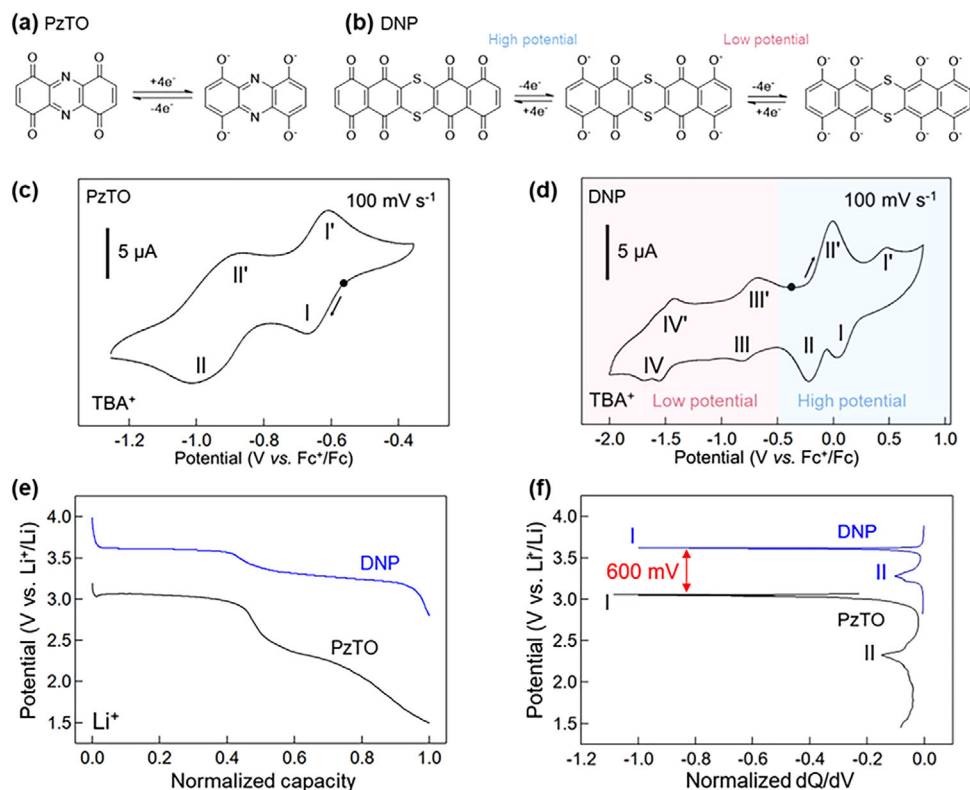


**FIGURE 2** | Electrochemical behavior of PzTO and DNP. (a,b) Schematic illustration of the molecular redox reaction pathways of (a) PzTO and (b) DNP. DNP undergoes an eight-electron reaction, with the first four electrons exchanged at high potential, while the remaining four electrons are exchanged at low potential. (c,d) Fourth-cycle cyclic voltammograms of 1 mM (c) PzTO and (d) DNP recorded in a three-electrode cell setup at a scan rate of  $100 \text{ mV s}^{-1}$  using 0.1 M TBAP in dimethylformamide as the electrolyte and ferrocene as an internal reference for molecular electrochemistry. Black circles indicate the starting point of the cycle. (e) Comparison of the first galvanostatic discharge curves of PzTO and DNP (high potential region only) recorded vs.  $\text{Li}^+/\text{Li}$  from coin cell measurements. (f) Corresponding normalized differential capacity ( $dQ/dV$ ) curves, highlighting the redox potential difference between PzTO and DNP in red.

comparably to an overall discharge capacity of  $375 \text{ mAh g}^{-1}$ , corresponding to 80% of the theoretical value. Notably, this capacity remains stable in the subsequent cycle, owing to the reduced solubility of DNP in the electrolyte, as evidenced by the colorless solution and the presence of undissolved species (Figure S7). Moreover, DNP exhibits lower voltage polarization (150 and 300 mV) than PzTO (200 and 600 mV) (Table S2). This reduced polarization is attributed to enhanced electronic percolation within the electrode composite, consistent with the relatively higher intrinsic electronic conductivity of DNP ( $7.88 \times 10^{-10} \text{ S cm}^{-1}$ , Figure S8) compared to PzTO ( $4.00 \times 10^{-12} \text{ S cm}^{-1}$ ) [46]. This interpretation is further supported by the superior rate capability of DNP relative to PzTO over a wide range of cycling rates (0.1C–2.0C) as shown in Figure S9.

A direct comparison of the potential vs. differential capacity ( $dQ/dV$ ) profiles (Figure 2f) further highlights the substantial potential difference between PzTO and DNP. Both compounds display an intense primary peak (I) and a secondary, less pronounced, shorter peak (II) at distinct potentials. PzTO operates at 3.08 and 2.30 V vs.  $\text{Li}^+/\text{Li}$ , while DNP operates at 3.68 and 3.30 V vs.  $\text{Li}^+/\text{Li}$ , reflecting a higher redox potential of DNP over PzTO by approximately 600 mV (Table S2). This voltage gap exceeds the value determined from molecular electrochemistry in a solvated phase (Figure 2d) by roughly 100 mV, underscoring the additional

influence of  $\text{Li}^+$  coordination and crystal packing effects on the observed redox potential.

## 3.2 | Electronic Structure Studies

### 3.2.1 | Comparative DFT Study of PzTO and DNP

To provide a theoretical understanding of the electrochemical behavior of PzTO and DNP, we performed DFT calculations. Using DFT, the reduction/oxidation processes are modeled as lithiation/delithiation processes, which are relevant to Nernst behavior as cathode materials for Li-ion batteries.

The computed lithiation and delithiation schemes and energetics are shown in Figure 3. Figure 3a,b shows schematic representations of the lithiation/delithiation reactions between zero and four Li atoms. The locations of the first two Li atoms in Figure 3a are determined based on the thermodynamic preference as discussed in Section S2, which compares energies of PzTO and DNP with every possible combination of two Li atoms. The same locations are consistently used for all proposed molecular derivatives throughout the manuscript, assuming similar thermodynamic trends. The schematics suggest two major molecular-level differences between PzTO and DNP: (1) molecular aromaticity and (2) Li-O coordination (vide infra).

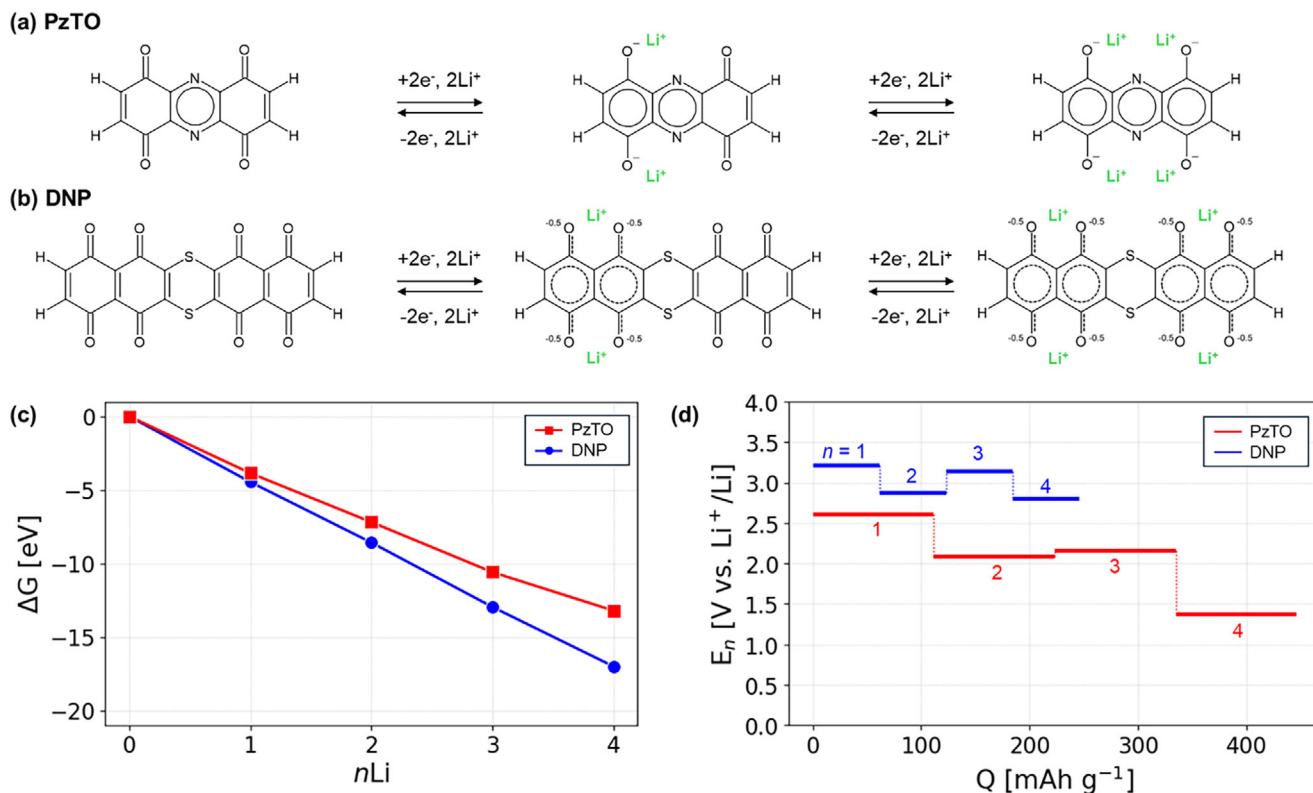


**FIGURE 3** | Schematics of lithiation/delithiation processes of (a) PzTO and (b) DNP from a bare molecule up to 4 Li uptake. Lithiation steps with the first and third Li are omitted for simplicity. Solid circles represent fully aromatic rings satisfying Hückel's rule (6  $\pi$  electrons) [64], while dotted lines and circles indicate partial bond character (intermediate between single and double bonds) and incomplete aromaticity due to insufficient  $\pi$  electrons, respectively. (c) DFT-computed lithiation Gibbs free energy profiles ( $\Delta G$ , eV) vs. number of Li ( $n\text{Li}$ ) and (d) reduction potential ( $E_n$ , V vs.  $\text{Li}^+/\text{Li}$ ) vs. specific charge capacity ( $Q$ ,  $\text{mAh g}^{-1}$ ) profiles of PzTO and DNP. Optimized molecular structures are shown in Figure S22.

First, the central ring of the bare PzTO molecule contains 6  $\pi$  electrons to satisfy Hückel's rule of aromaticity [64], and the two other rings also become aromatic upon reduction with 4 Li (Figure 3a). On the other hand, none of the five rings of the DNP molecule attains enough  $\pi$  electrons to be fully aromatic throughout the lithiation process between 0 and 4 Li atoms (Figure 3b). All rings except the central 1,4-dithiin ring can be aromatic with 4 additional electrons; however, DNP with more than 4 Li atoms is not simulated in this work since a single molecule with a high level of lithiation involves significant structural distortion, so that the model is not relevant to experimental observations (Section S5 visualizes geometric distortion associated with the high levels of lithiation). Another major difference is the number of O atoms that each Li coordinates ( $\text{CN}_{\text{Li-O}}$ ); PzTO has four carbonyl redox centers ( $\text{C}=\text{O}$ ), each of which is taken by one Li, whereas DNP contains four pairs of two neighboring carbonyl oxygens, resulting in each Li being coordinated with two. While Li atoms can also coordinate with the N heteroatoms in similar molecular systems [65], the Li-N interactions in PzTO are notably weaker than the Li-O interactions, as discussed in Section S6. Therefore, we focus on  $\text{CN}_{\text{Li-O}}$  as the primary structural distinction between PzTO and DNP. Although PzTO and DNP feature different heteroatoms, their electronic effects do not govern redox potentials, considering that PzTO, with a more electronegative element ( $N \sim 3.04$ ), exhibits a lower voltage than DNP ( $S \sim 2.58$ ) [40]. In summary, they are compared as follows:

PzTO (highly aromatic,  $\text{CN}_{\text{Li-O}} = 1$ ) vs. DNP (less aromatic,  $\text{CN}_{\text{Li-O}} = 2$ ).

The computed lithiation Gibbs free energy profiles ( $\Delta G$ , eV) of PzTO and DNP are displayed in Figure 3c. Throughout the reduction (lithiation) process, DNP exhibits consistently more exergonic energetics compared to PzTO. The calculations were repeated for higher spin states, which confirmed that spin crossover (a change in the ground spin state from low to high or vice versa) is unlikely to occur or alter the energy profiles (see Section S7). In Figure 3d, the free energy profiles are converted into a reduction potential ( $E_n$ ) vs. specific charge capacity curves using Equations (1) and (2). The redox potential of DNP is at  $\sim 3$  V vs.  $\text{Li}^+/\text{Li}$  (up to 4 Li), whereas that of PzTO starts at 2.6 V and decreases to 1.4 V upon lithiation. The redox potential profiles show a systematic negative shift from the experimental discharge curves (Figure 2e) by  $\sim 0.6$  V. This is attributed to the different polarization environments (i.e., implicit solvation in molecular DFT vs. crystal-state environment in experiments) and the omission of crystal packing effects, such as favorable interstitial or interlayer Li sites that can further stabilize the lithiated states that can be identified using periodic DFT calculations [66]. The lower specific charge capacity of DNP (up to 250  $\text{mAh g}^{-1}$ ) than PzTO is due to the limited number of Li atoms (maximum of 4) as described above; note that a larger specific capacity of DNP was predicted ( $\sim 491$   $\text{mAh g}^{-1}$ ) from periodic DFT calculations, which corresponds to 8 Li uptake [66].

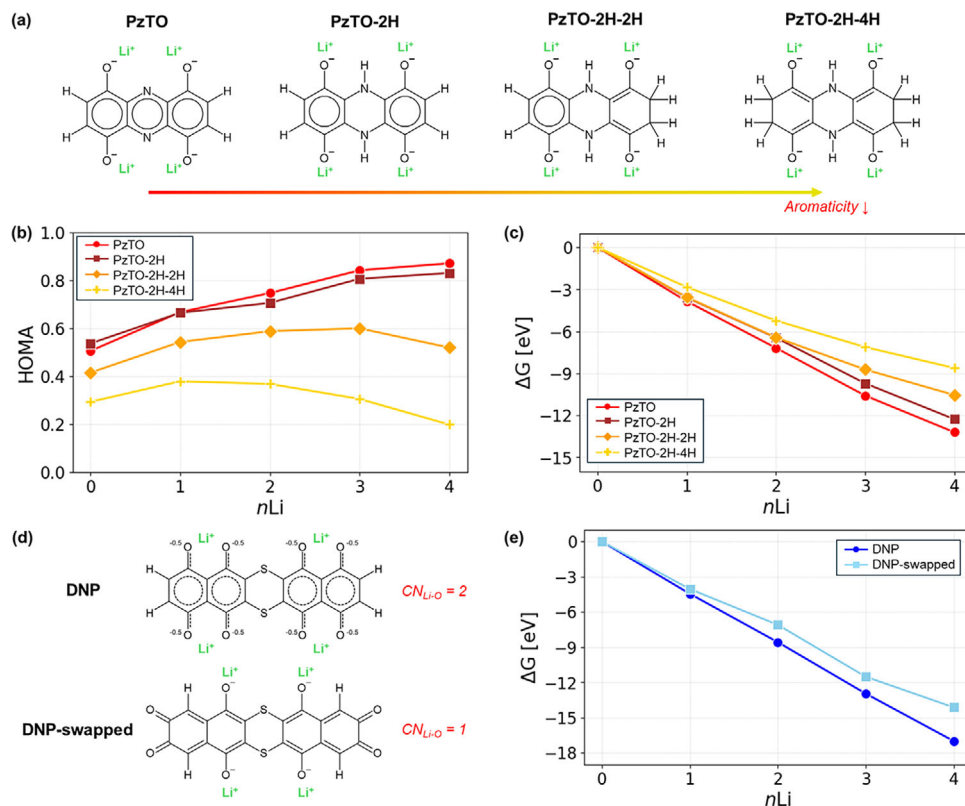


**FIGURE 4** | (a) Chemical structures of lithiated (4 Li) PzTO and its derivatives based on hydrogenation (PzTO-2H, PzTO-2H-2H, and PzTO-2H-4H) with molecular aromaticity decreasing from left to right. (b) Harmonic Oscillator Model of Aromaticity (HOMA) and (c) Gibbs free energy ( $\Delta G$ , eV) profiles during lithiation (1–4) of the PzTO family in panel (a) vs. number of Li ( $n\text{Li}$ ). (d) Chemical structures of lithiated DNP and its derivative prepared by swapping hydrogen atoms with their closest oxygen atoms (DNP-swapped), with their Li–O coordination number ( $\text{CN}_{\text{Li-O}}$ ). (e)  $\Delta G$  profiles of the DNP family in panel (d) vs.  $n\text{Li}$ . Optimized molecular structures are shown in Figures S22–S24.

### 3.2.2 | Elucidating Roles of Aromaticity and Li-O Coordination

In Section 3.2.1, we identified two molecular-level features, aromaticity and  $\text{CN}_{\text{Li-O}}$ , which could explain the distinct redox potential difference between PzTO and DNP. Here, we explored hypothetical PzTO- and DNP-derivatives by modulating the molecular aromaticity (in PzTO) and  $\text{CN}_{\text{Li-O}}$  (in DNP), in order to investigate their respective contributions to redox behaviors.

The reduced PzTO molecule with 4 Li is aromatic, as shown in Figure 3a. This aromatic conjugated system can be disrupted by partial hydrogenation without significant deviation in the molecular structure. Figure 4a shows the chemical structures of PzTO and its derivatives with additional hydrogen atoms: two on the central ring (PzTO-2H), two more on the right ring (PzTO-2H-2H), and another two more on the left ring (PzTO-2H-4H). As more hydrogen atoms are introduced, the overall aromaticity of the molecule is expected to decrease accordingly, as illustrated in the molecular representations in Figure S13. Aromaticity is quantified using HOMA based on the DFT-optimized molecular geometries (Figure 4b) [58–60]. A bare PzTO molecule is moderately aromatic ( $\sim 0.5$ ), but the aromaticity increases as being lithiated, as expected from the lithiation schematics (Figure 3a). The HOMA profiles of the PzTO family (Figure 4b) show that aromaticity decreases with increasing hydrogen content, with the effect being more pronounced at higher lithiation levels.

The lithiation free energy (Figure 4c) becomes less exergonic as the hydrogenation level increases, which corresponds to a decrease in aromaticity. This trend may be associated with the capability of conjugated structures to delocalize the transferred electrons upon reduction, thereby stabilizing the reduced phase [67]. These results might suggest a straightforward positive correlation between aromaticity and reduction potential; however, Section 3.3 discusses a more accurate role of aromaticity.

Figure 4d shows an engineered DNP-derivative, “DNP-swapped”, which is prepared by swapping the four H atoms (attached to the leftmost and rightmost carbon atoms) with their nearest O atoms. During lithiation, Li atoms are added to the carbonyl oxygen atoms close to the central dithiin ring. As a result, the  $\text{CN}_{\text{Li-O}}$  of DNP-swapped is fixed at 1, which is smaller than that of DNP ( $\text{CN}_{\text{Li-O}} = 2$ ; see Figure 4d). The HOMA of DNP monotonically increases during lithiation (Figure S14; HOMA profiles), consistent with the additional electrons being accommodated in the conjugated core and reducing C–C bond-length alternation, as supported by the frontier-orbital analysis and C–C bond-length changes in Figure S15. DNP-swapped exhibit similar electronic structures with DNP, as evidenced by their nearly identical molecular aromaticity (Figure S14) and LUMO energy levels (Figure S16). Despite this similarity, DNP exhibits a significantly more exergonic lithiation free energy profile compared to DNP-swapped (Figure 4e). For example, the lithiation free energy for the addition of 4 Li atoms ( $\Delta G_4$ ) for DNP is shifted by +2.87 eV

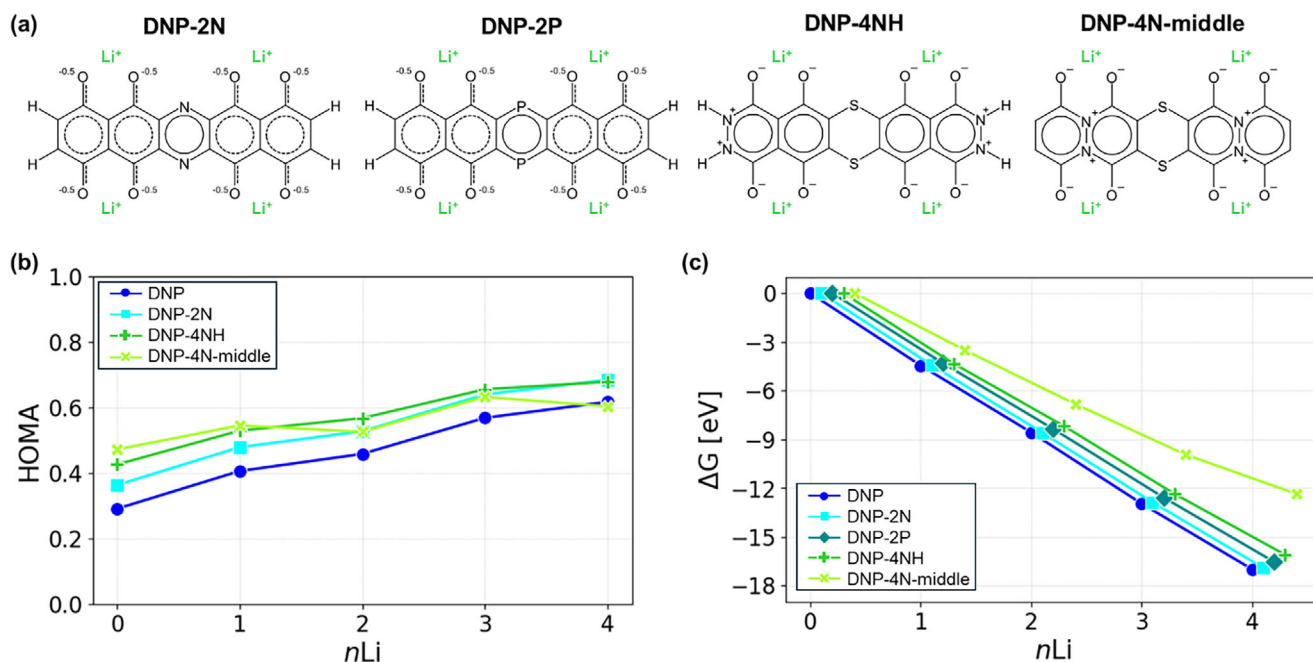


**FIGURE 5** | (a) Chemical structures of lithiated (4 Li) DNP-derivatives with different levels of molecular aromaticity modulated by heteroatoms. (b) HOMA and (c) Gibbs free energy ( $\Delta G$ , eV) profiles during lithiation of the DNP and DNP-derivatives in panel (a) vs. number of Li ( $n\text{Li}$ ). A HOMA profile for DNP-2P is not shown in panel (b) since HOMA parameters were not defined for P [61]. Small x-axis offsets are applied in panel (c) to avoid overlap. Optimized molecular structures are shown in Figure S25.

(i.e., less exergonic) due to the molecular modification. These observations clearly demonstrate that a higher  $\text{CN}_{\text{Li-O}}$  leads to greater Li affinity, thereby improving reduction potentials.

### 3.3 | Leveraging Molecular Engineering Strategies

In Section 3.2, we identified two molecular features that are associated with their reduction potentials via comparative DFT calculations: aromaticity (chemical descriptor) and Li-O coordination (structural descriptor). In the following sections, we leverage these features on PzTO and DNP to improve their redox potentials. In addition, we explore a conventional electron-withdrawing functionalization approach [33, 36, 39, 68] to establish its role in improving the redox potentials of PzTO and DNP.

#### 3.3.1 | Modulating Aromaticity

In Section 3.2.2, we observed a positive correlation between aromaticity and reduction potential among the PzTO family. DNP exhibits lower aromaticity (HOMA values: 0.3–0.6; Figure S14) than PzTO (0.5–0.9; Figure 4b), because the former lacks  $\pi$  electrons to satisfy Hückel's rule for aromaticity. Hence, we hypothesize that the reduction potential of DNP can be improved by providing additional electrons. This can be done via elemental substitution, replacing existing atoms with another type of atom that has one extra valence electron. To test this hypothesis, we designed two derivatives of DNP as shown in Figure 5a: DNP-2N and DNP-2P, which are prepared by replacing the central sulfur with nitrogen (N) atoms and phosphorus (P) atoms, respectively. Both N and P atoms introduce one more  $\pi$  electron than S,

leading to an increased aromaticity in the central ring (Figure 5a). The N-substitution increases HOMA by 0.07 throughout the lithiation process (Figure 5b). The HOMA change due to the P-substitution could not be quantified because the parameters are not defined for P [61]. However, neither substitution improves the reduction potential: DNP-2N shows no change, and DNP-2P exhibits slightly decreased lithiation exergonicity, compared to the original DNP (Figure 5c).

We posit that increasing aromaticity in the central ring has minimal impact on the reduction potential because the central ring is relatively far from the redox centers, which limits effective electron delocalization. To investigate this, we prepared two additional derivatives: DNP-4NH and DNP-4N-middle, by substituting the outermost and middle 4 C atoms with N atoms, respectively (Figure 5a). Since N has one more valence electron than C, these substitutions increase the aromaticity of the structure. The increase in aromaticity is significant (DNP-4NH and DNP-4N-middle have higher HOMA than DNP by 0.14 and 0.18, respectively, in Li-free molecules), although the effect lessens at higher levels of lithiation (Figure 5b). Still, the lithiation free energies of these derivatives are less exergonic than those of the original DNP molecule (Figure 5c).

These DFT calculations indicate that simply increasing the aromaticity of the molecular backbone by adding extra electrons does not necessarily improve the reduction potential, contrary to our initial hypothesis. Figure 6a shows the lithiation free energy vs. HOMA change associated with the addition of four Li atoms ( $\Delta G_4$  vs.  $\Delta\text{HOMA}_4$ ) of DNP and its derivatives shown in Figure 5a. Interestingly, we identified a clear inverse linear relationship: a greater increase in HOMA corresponds to a more exergonic lithiation free energy. This clearly shows that the governing factor

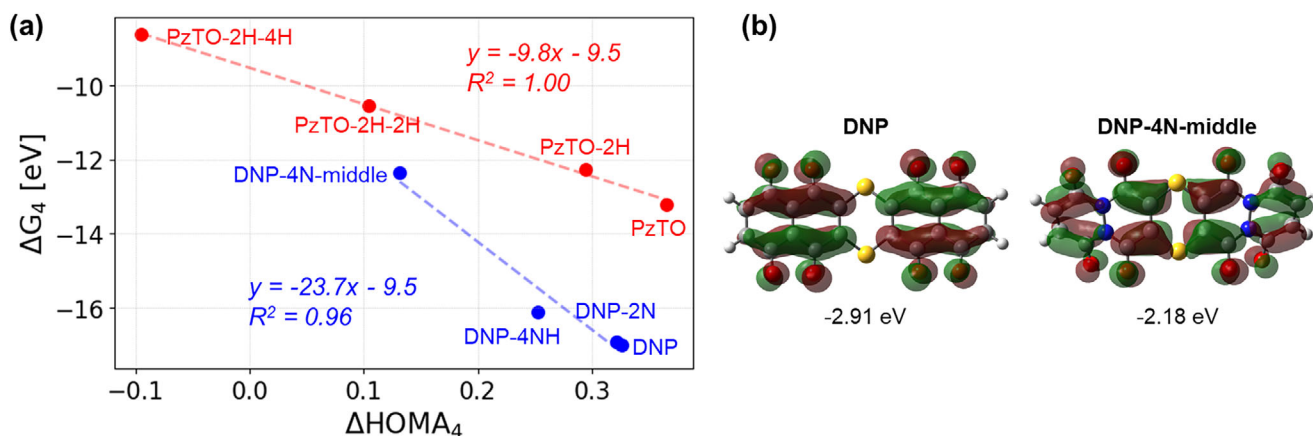


**FIGURE 6** | (a) Linear relationship between lithiation free energies ( $\Delta G_4$ ) and HOMA difference ( $\Delta \text{HOMA}_4$ ) upon lithiation with 4 Li for the PzTO family shown in Figure 4a (red) and DNP family shown in Figure 4d (blue). (b) Visualized LUMO of DNP and DNP-4N-middle with their energy levels.

in controlling reduction potential is not the absolute aromaticity of a molecule; rather, the extent to which aromaticity changes during lithiation is closely correlated with the reduction energetics. Although the elemental substitutions in Figure 5a effectively increase the absolute HOMA value at each lithiation state, the overall HOMA change over lithiation decreases, resulting in less exergonic lithiation free energy profiles. The greater aromaticity gain ( $\Delta \text{HOMA}$ ) indicates more effective delocalization of extra electrons obtained upon reduction, thereby stabilizing the reduced state. This trend is qualitatively consistent with the LUMO energy (Figure 6b); for example, DNP-4N-middle (low  $\Delta \text{HOMA}$ ) exhibits a higher LUMO energy level than DNP (high  $\Delta \text{HOMA}$ ), which is attributed to the disruption of  $\pi$ -delocalization across the fused-ring backbone by N substitution. Nevertheless, as exemplified by the comparison between DNP and DNP-swapped in Section S10, the LUMO energies of Li-free molecules fail to capture the redox behaviors associated with lithiation, demonstrating the advantage of  $\Delta \text{HOMA}$  over LUMO energy.

Note that the linear relationship between lithiation free energy and  $\Delta \text{HOMA}$  holds across the various heteroatom-derivatives of DNP. This suggests that  $\Delta \text{HOMA}$  can serve as a quantifiable descriptor for reported heteroatom effects on redox potentials [38, 40, 41]. Figure 6a shows that such an inverse linear relationship holds true among the PzTO family shown in Figure 4a, confirming the crucial role of  $\Delta \text{HOMA}$ . Interestingly, each molecular family displays its own relationship with significantly different slopes. This indicates that  $\Delta \text{HOMA}$  is dependent on a core structure, and therefore it may not serve as a global descriptor, such as LUMO energies (Figure S16 shows a linear relationship between first reduction potential and LUMO energy of PzTO and DNP families in Figure 4a,d) [69, 70].

Wu et al. [71] also observed a positive correlation between aromaticity change (based on Clar's sextet rule [72, 73]) vs. reduction potential upon the addition of two Li atoms across several polycyclic compounds. While their work observed trends across different numbers and arrangements of cyclic units, our results indicate that differential aromaticity serves as a quantifiable descriptor within the same family of molecules. Taken

together, these observations lead us to a refined version of the first strategy: to improve the reduction potential, molecules should be designed to exhibit a greater increase in aromaticity upon reduction.

### 3.3.2 | Increasing Li–O Coordination Number

Another key feature identified in Section 3.2.2 is Li–O coordination number,  $\text{CN}_{\text{Li-O}}$ . This can be increased by replacing existing atoms or molecular fragments with oxygen-containing functional groups. Accordingly, we explored three PzTO derivatives: (1) PzTO-4CHO, where all hydrogen atoms are replaced with formyl ( $-\text{CHO}$ ) groups; (2) PzTO-2NO<sub>2</sub>, where two hydrogen atoms are replaced with nitro ( $-\text{NO}_2$ ) groups; and (3) PzTO-2SO<sub>2</sub>, where the central nitrogen atoms are replaced with sulfonyl ( $-\text{SO}_2-$ ) groups. See Figure 7a for their chemical structures. Note that more than two nitro groups are not considered as they introduce repulsive interactions. All three derivatives show similar improvements in lithiation thermodynamics, where the free energy for the addition of 4 Li ( $\Delta G_4$ ) becomes more exergonic by 2.5–2.8 eV (Figure 7c). The absolute lithiation energies of these PzTO-derivatives ( $\Delta G_4 = -15.7$  to  $-16.0$  eV) are slightly less exergonic than that of DNP ( $\Delta G_4 = -17.0$  eV). However, they may offer potential advantages in terms of energy density due to their lighter molecular weights compared to DNP (330.2–352.2 g mol<sup>-1</sup> for PzTO derivatives vs. 436.4 g mol<sup>-1</sup> for DNP). Unlike PzTO, the introduction of additional Li–O coordination into DNP through functionalization is challenging, as discussed in Section S12. This may indicate that  $\text{CN}_{\text{Li-O}} = 2$  is optimal for achieving high redox potentials at the molecular level.

The impact of the functionalization on aromaticity is noteworthy (Figure 7b). Compared to pristine PzTO, the formyl and nitro groups decrease the HOMA values at high lithium loadings, leading to reduced differential aromaticity. Conversely, the sulfonyl group results in higher differential aromaticity due to the lower HOMA values at low lithium loadings. Despite these differences, all derivatives exhibit comparable lithiation free energy profiles. This suggests that controlling one feature ( $\text{CN}_{\text{Li-O}}$ ) can affect the other (differential aromaticity), and that their collective behavior determines lithiation energetics.

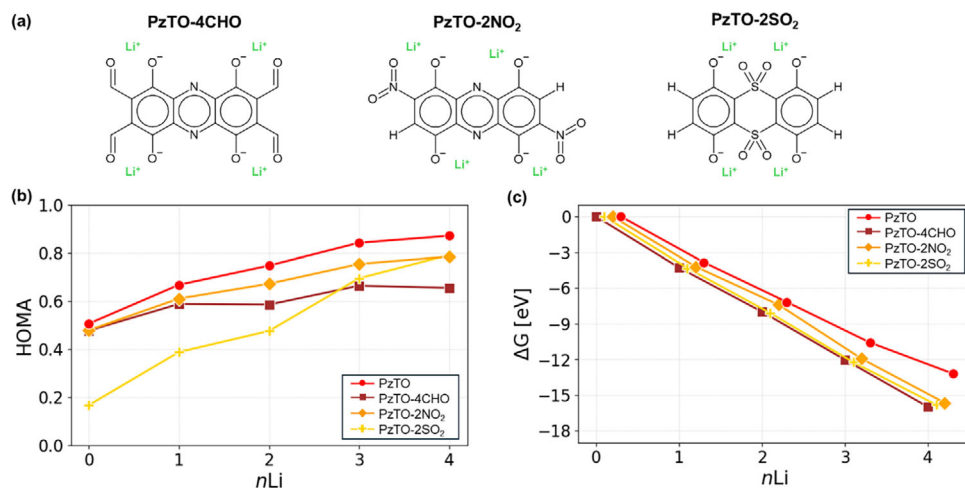


**FIGURE 7** | (a) Chemical structures of lithiated (4 Li) PzTO-derivatives prepared by functionalizing with oxo-containing groups to increase Li–O coordination. (b) HOMA and (c) Gibbs free energy profiles during lithiation of the PzTO and PzTO-derivatives in panel (a) vs. number of Li ( $n\text{Li}$ ). Small x-axis offsets are applied in panel (c) to avoid overlap. Optimized molecular structures are shown in Figure S26. Section S11 discusses changes in the orientation of formyl functional groups of PzTO-4CHO during lithiation.

### 3.3.3 | Electron-Withdrawing Functionalization

Electron-withdrawing groups (EWGs) are known to stabilize the electrons acquired during reduction, thereby improving redox potentials [33, 36, 37, 39, 68]. First, we replaced hydrogen atoms of DNP and PzTO with fluorine (–F) and cyano (–CN) functional groups. As shown in Figure S20, both yield more exergonic lithiation free energy profiles for DNP and PzTO, with the cyano group producing greater improvement, due to its stronger electron-withdrawing nature. See Section S13 for details.

We also explored tetraaza-functionalization by substituting the two C–H moieties at both ends of DNP and PzTO with nitrogen atoms, denoted as DNP-4N-side and PzTO-4N, respectively (Figure 8a). Due to the high electronegativity of nitrogen, this modification promotes electron delocalization, similar to EWGs [38, 41]. Figure 8b compares the spin population of DNP and DNP-4N-side molecules, each paired with 1 Li atom (doublet spin state), illustrating the stabilizing role of N on the additional electron acquired upon reduction. The tetraaza-functionalization leads to more exergonic lithiation free-energy profiles (Figure 8c,d);  $\Delta G_4$  of DNP and PzTO negatively shift (more exergonic) by 1.2 and 3.4 eV, respectively. Notably, HOMA values at low lithiation levels decrease more substantially than those at higher levels upon tetraaza-functionalization, resulting in a larger differential aromaticity. The linear relationship between differential aromaticity and lithiation exergonicity shown in Figure 6a is reproduced with these tetraaza derivatives in Figure S21, where the linearity remains unchanged. This confirms the role of the differential aromaticity discussed in Section 3.3.1.

The tetraaza-functionalization (Figure 8) yields comparable improvement in the lithiation energetics to the cyano-functionalization (Figure S20) for both DNP and PzTO. It is worth noting that, however, the tetraaza derivatives are much lighter than the cyano derivatives in terms of molecular mass, by 18% and 28% for DNP and PzTO, respectively. This suggests that heteroatom substitution can offer more favorable options over

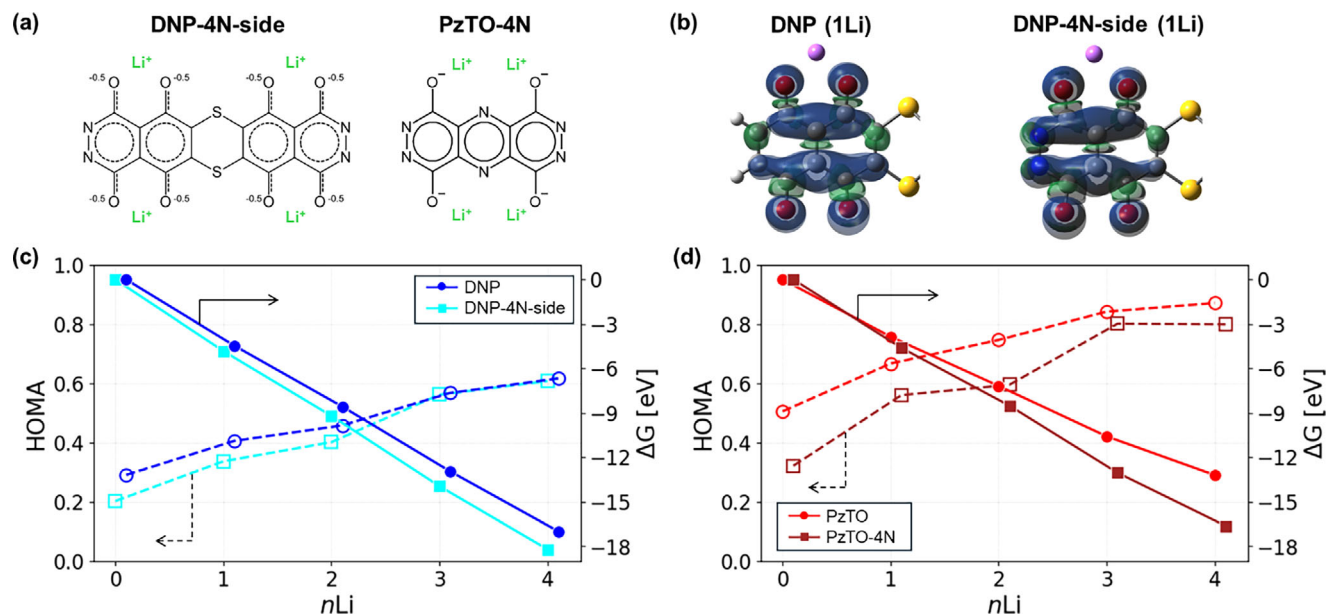
EWG addition in terms of specific charge capacity and energy density.

### 3.3.4 | Summary of Molecular Design Strategies

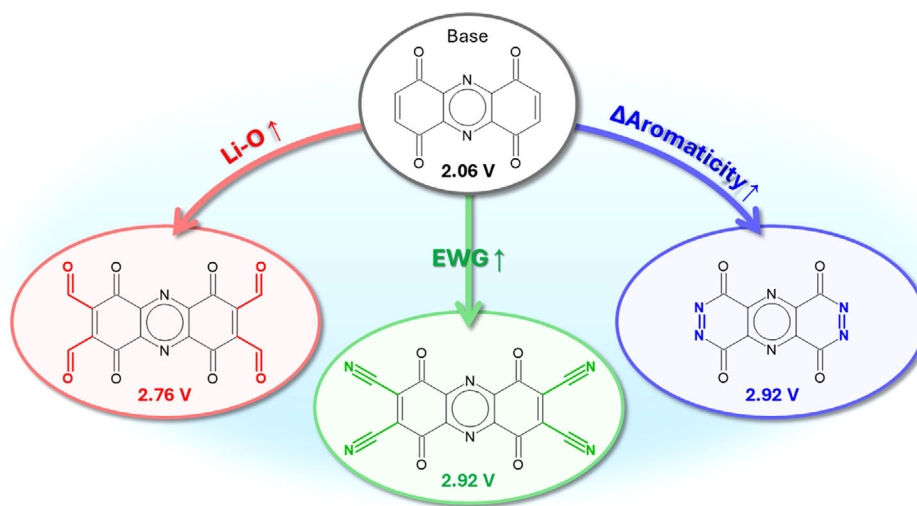
In this work, we discussed three molecular design strategies as summarized in Figure 9, using PzTO as an example: (1) introducing additional Li–O coordination, (2) increasing differential aromaticity, and (3) adding EWGs. Corresponding average reduction potentials for 0–4 Li uptake ( $\Delta\bar{E}$ ) are also provided.

Figure 9 shows a greater increase in average reduction potential by additional EWG and larger differential aromaticity ( $\Delta\bar{E} = 0.86\text{ V}$ ) than increased Li–O coordination ( $\Delta\bar{E} = 0.70\text{ V}$ ). However, this trend is specific to the examples considered and is not necessarily universal. As discussed, the functional groups introduced to increase Li–O coordination of PzTO in Figure 7 (i.e., –CHO, –NO<sub>2</sub>, and –SO<sub>2</sub>–) provide markedly different effects on differential aromaticity, yet yield nearly identical reduction free-energy profiles. Furthermore, even though formyl groups result in a smaller improvement in reduction potential than tetraaza-functionalization, the formyl-functionalized PzTO can theoretically host up to 8 Li (one Li per oxygen), providing a potential advantage in capacity compared to the tetraaza derivative (up to 4 Li). Hence, these strategies should be considered comprehensively, with the optimal choice conditioned on the base molecular framework.

It is also worth noting that these strategies are not mutually exclusive. For instance, the greater differential aromaticity reflects a stronger ability of the backbone to stabilize additional electrons acquired during reduction, and EWGs raise the reduction potential through the same underlying principle (i.e., enhancing electron affinity) [33, 36, 37, 39, 68]. They only differ in the position of electron accommodation, backbone vs. substituent, with the former manifesting as greater differential aromaticity. Also, the functional groups introduced to promote Li–O coordination in Section 3.3.2 are themselves electron-



**FIGURE 8** | (a) Chemical structures of tetraaza-functionalized derivatives of DNP (DNP-4N-side) and PzTO (PzTO-4N). (b) Visualized spin density of DNP and DNP-4N-side with one Li atom (isovalue =  $4e-4$ ). The right half of the structures (naphthazarin) is trimmed for simplicity (no spin population). HOMA (dashed line) and lithiation Gibbs free energy (solid line) profiles of (c) DNP and DNP-4N-side and (d) PzTO and PzTO-4N vs. number of Li ( $n\text{Li}$ ). Small x-axis offsets are applied in panels (c) and (d) to avoid overlap. Optimized molecular structures are shown in Figures S27 and S28.



**FIGURE 9** | Molecular engineering strategies illustrated with PzTO and its derivatives as an example. “Li–O,” “EWG,” and “ $\Delta$ Aromaticity” stand for Li–O coordination, electron-withdrawing group, and differential aromaticity, respectively. Average reduction potentials (V) up to 4 Li uptake are provided.

withdrawing. Thus, the improvement in lithiation free energies observed in Figure 7 can be partly attributed to the EWG character of these substituents. Overall, these strategies are complementary and may act synergistically, rather than functioning independently.

An important next step will be to assess the applicability of the suggested molecular-level descriptors to a broader range of organic electrode materials, such as non-carbonyl compounds and polymeric systems. Beyond this molecular-level question,

key bottlenecks remain in the synthesizability of newly proposed molecules and their performance at the crystal and electrode levels. Recent progress in predicting the synthesizability [74, 75] and crystal structures [76, 77] of organic materials raises the prospect of an *in silico* discovery loop for novel organic cathodes, which can be followed by experimental validation for a limited set of the best candidates. In this context, the strategies proposed here provide actionable guidelines for rationally assembling a large pool of candidate molecules as a first step toward such efforts.

## 4 | Conclusion

In this manuscript, we investigated two carbonyl-based organic cathode materials, PzTO and DNP, to resolve molecular-level origins of their distinct redox behaviors. Combined electrochemistry and DFT lithiation modeling provided insights into their different redox behaviors and identified two key descriptors: molecular aromaticity and Li–O coordination. Based on systematic exploration of hypothetical molecular derivatives of PzTO and DNP, we proposed two molecular engineering strategies for increasing their reduction potentials: (i) increasing differential aromaticity (aromaticity gain upon reduction, e.g.,  $\Delta\text{HOMA}$ ), and (ii) increasing Li–O coordination. We also evaluated a conventional approach of adding electron-withdrawing substituents and confirmed the strong influence of electronic modulation on reduction energetics. Both increasing differential aromaticity and adding electron-withdrawing substituents improve the reduction potential (e.g., a potential increase of 0.86 V for PzTO). The influence of additional Li–O coordination is less profound on the reduction potential (e.g., a potential increase of 0.70 V for PzTO); however, it provides an advantage in capacity and energy density by allowing the accommodation of extra Li atoms. Importantly, we demonstrated that these strategies could work synergistically rather than being mutually exclusive. Overall, the proposed molecular engineering strategies shed light on the origin of the redox behaviors of reported materials and extract underlying principles, thereby providing actionable guidelines for the future exploration of a vast design space of organics toward the discovery of synthesizable, high-performing cathode materials.

### Acknowledgements

This work was supported by the Energy Storage Research Alliance “ESRA” (DE-AC02-06CH11357), an Energy Innovation Hub funded by the U.S. Department of Energy, Office of Science, Basic Energy Sciences. S.H. and R.S.A. acknowledge computational support from the Center for Nanoscale Materials, a U.S. Department of Energy Office of Science User Facility, supported by the U.S. DOE, Office of Basic Energy Sciences, under Contract No. DE-AC02-06CH11357 (User proposal No. 83823).

### Conflicts of Interest

Y.Y. has equity interests in LiBeyond, LLC and Solid Design Instruments, LLC. The University of Houston reviewed and approved his relationship in compliance with its conflict-of-interest policy. The remaining authors declare no competing interests.

### Data Availability Statement

The data that supports the findings of this study are available in the supplementary material of this article.

### References

1. P. Poizot, J. Gaubicher, S. Renault, L. Dubois, Y. Liang, and Y. Yao, “Opportunities and Challenges for Organic Electrodes in Electrochemical Energy Storage,” *Chemical Reviews* 120, no. 14 (2020): 6490–6557, <https://doi.org/10.1021/acs.chemrev.9b00482>.
2. A. Innocenti, H. Adenusi, and S. Passerini, “Assessing n-Type Organic Materials for Lithium Batteries: A Techno-Economic Review,” *InfoMat* 5, no. 11 (2023): 12480, <https://doi.org/10.1002/inf2.12480>.

3. J. Kim, Y. Kim, J. Yoo, G. Kwon, Y. Ko, and K. Kang, “Organic Batteries for a Greener Rechargeable World,” *Nature Reviews Materials* 8, no. 1 (2023): 54–70, <https://doi.org/10.1038/s41578-022-00478-1>.
4. B. Häupler, A. Wild, and U. S. Schubert, “Carbonyls: Powerful Organic Materials for Secondary Batteries,” *Advanced Energy Materials* 5, no. 11 (2015): 1402034, <https://doi.org/10.1002/aenm.201402034>.
5. S. Muench, A. Wild, C. Friebe, B. Häupler, T. Janoschka, and U. S. Schubert, “Polymer-Based Organic Batteries,” *Chemical Reviews* 116, no. 16 (2016): 9438–9484, <https://doi.org/10.1021/acs.chemrev.6b00070>.
6. Q. Zhao, Z. Zhu, and J. Chen, “Molecular Engineering With Organic Carbonyl Electrode Materials for Advanced Stationary and Redox Flow Rechargeable Batteries,” *Advanced Materials* 29, no. 48 (2017): 1607007, <https://doi.org/10.1002/adma.201607007>.
7. B. Esser, F. Dolhem, M. Becuwe, P. Poizot, A. Vlad, and D. Brandell, “A Perspective on Organic Electrode Materials and Technologies for Next Generation Batteries,” *Journal of Power Sources* 482 (2021): 228814, <https://doi.org/10.1016/j.jpowsour.2020.228814>.
8. Y. Lu and J. Chen, “Prospects of Organic Electrode Materials for Practical Lithium Batteries,” *Nature Reviews Chemistry* 4, no. 3 (2020): 127–142, <https://doi.org/10.1038/s41570-020-0160-9>.
9. L. Zhao, A. E. Lakraychi, Z. Chen, Y. Liang, and Y. Yao, “Roadmap of Solid-State Lithium–Organic Batteries Toward 500 Wh kg<sup>−1</sup>,” *ACS Energy Letters* 6, no. 9 (2021): 3287–3306, <https://doi.org/10.1021/acsenergylett.1c01368>.
10. H. Dai, L. Guan, M. Mao, and C. Wang, “Evaluating the Present and Future of Organic Batteries,” *Nature Reviews Clean Technology* 1 (2025): 493–510.
11. J. Bitenc, K. Pirnat, O. Luzanin, and R. Dominko, “Organic Cathodes, a Path Toward Future Sustainable Batteries: Mirage or Realistic Future?,” *Chemistry of Materials* 36, no. 3 (2024): 1025–1040, <https://doi.org/10.1021/acs.chemmater.3c02408>.
12. W. Li, E. M. Erickson, and A. Manthiram, “High-Nickel Layered Oxide Cathodes for Lithium-Based Automotive Batteries,” *Nature Energy* 5, no. 1 (2020): 26–34, <https://doi.org/10.1038/s41560-019-0513-0>.
13. A. Manthiram, “A Reflection on Lithium-Ion Battery Cathode Chemistry,” *Nature Communications* 11, no. 1 (2020): 1550, <https://doi.org/10.1038/s41467-020-15355-0>.
14. Y. Lu, Q. Zhang, F. Li, and J. Chen, “Emerging Lithiated Organic Cathode Materials for Lithium-Ion Full Batteries,” *Angewandte Chemie* 135, no. 7 (2023): 202216047, <https://doi.org/10.1002/ange.202216047>.
15. A. Jouhara, N. Dupré, A.-C. Gaillot, D. Guyomard, F. Dolhem, and P. Poizot, “Raising the Redox Potential in Carboxyphenolate-Based Positive Organic Materials via Cation Substitution,” *Nature Communications* 9, no. 1 (2018): 4401, <https://doi.org/10.1038/s41467-018-06708-x>.
16. J. Wang, A. E. Lakraychi, X. Liu, et al., “Conjugated Sulfonamides as a Class of Organic Lithium-Ion Positive Electrodes,” *Nature Materials* 20, no. 5 (2021): 665–673, <https://doi.org/10.1038/s41563-020-00869-1>.
17. A. Jouhara, E. Quarez, N. Gautier, et al., “Unveiling the Peierls Effect During Electrochemical Delithiation/Lithiation Process in Magnesium (2,5-dilithium-oxy)-Terephthalate Using Combined Experimental and Computational Studies,” *Energy Storage Materials* 81 (2025): 104456, <https://doi.org/10.1016/j.ensm.2025.104456>.
18. T. Yokoji, H. Matsubara, and M. Satoh, “Rechargeable Organic Lithium-Ion Batteries Using Electron-Deficient Benzoquinones as Positive-Electrode Materials With High Discharge Voltages,” *Journal of Materials Chemistry A* 2, no. 45 (2014): 19347–19354, <https://doi.org/10.1039/C4TA02812K>.
19. W. Deng, W. Shi, P. Li, et al., “A Li-Contained Air-Stable Cathode for High-Performance All-Organic Lithium-Ion Batteries,” *Energy Storage Materials* 46 (2022): 535–541, <https://doi.org/10.1016/j.ensm.2022.01.039>.
20. Y. Katsuyama, H. Kobayashi, K. Iwase, Y. Gambe, and I. Honma, “Are Redox-Active Organic Small Molecules Applicable for High-Voltage

- (>4 V) Lithium-Ion Battery Cathodes?," *Advanced Science* 9, no. 12 (2022): 2200187.
21. Y. Gambe, H. Kobayashi, and I. Honma, "A 3.5 V-Class Organic Sodium-Ion Battery Using a Croconate Cathode," *Chemical Engineering Journal* 479 (2024): 147760, <https://doi.org/10.1016/j.cej.2023.147760>.
22. L. Huang, Z. Hu, M. Li, et al., "Trilithium Salt of Tetrahydroxyanthraquinone: A High-Voltage and Stable Organic Cathode Material for Rechargeable Lithium Metal and Lithium-Ion Batteries," *Chemical Engineering Journal* 481 (2024): 148447, <https://doi.org/10.1016/j.cej.2023.148447>.
23. A. L. Barrès, J. Geng, G. Bonnard, et al., "High-Potential Reversible Li Deintercalation in a Substituted Tetrahydroxy-p-benzoquinone Dilithium Salt: An Experimental and Theoretical Study," *Chemistry—A European Journal* 18, no. 28 (2012): 8800–8812.
24. Y. Hanyu, Y. Ganbe, and I. Honma, "Application of Quinonic Cathode Compounds for Quasi-Solid Lithium Batteries," *Journal of Power Sources* 221 (2013): 186–190, <https://doi.org/10.1016/j.jpowsour.2012.08.040>.
25. T. Liu, M.-M. Liu, X.-W. Zheng, et al., "Substituent Effects on the Redox Potentials of Dihydroxybenzenes: Theoretical and Experimental Study," *Tetrahedron* 70, no. 47 (2014): 9033–9040, <https://doi.org/10.1016/j.tet.2014.10.020>.
26. T. Yokoji, Y. Kameyama, N. Maruyama, and H. Matsubara, "High-Capacity Organic Cathode Active Materials of 2, 2'-bis-p-benzoquinone Derivatives for Rechargeable Batteries," *Journal of Materials Chemistry A* 4, no. 15 (2016): 5457–5466, <https://doi.org/10.1039/C5TA10713J>.
27. A. E. Lakraychi, E. Deunf, K. Fahsi, et al., "An Air-Stable Lithiated Cathode Material Based on a 1, 4-benzenedisulfonate Backbone for Organic Li-Ion Batteries," *Journal of Materials Chemistry A* 6, no. 39 (2018): 19182–19189, <https://doi.org/10.1039/C8TA07097K>.
28. D. Rambabu, A. E. Lakraychi, J. Wang, et al., "An Electrically Conducting Li-Ion Metal–Organic Framework," *Journal of the American Chemical Society* 143, no. 30 (2021): 11641–11650, <https://doi.org/10.1021/jacs.1c04591>.
29. Y. Zhang, J. Wang, P. Apostol, et al., "Bimetallic Anionic Organic Frameworks With Solid-State Cation Conduction for Charge Storage Applications," *Angewandte Chemie* 135, no. 42 (2023): 202310033, <https://doi.org/10.1002/ange.202310033>.
30. S. Gottis, A.-L. Barrès, F. Dolhem, and P. Poizot, "Voltage Gain in Lithiated Enolate-Based Organic Cathode Materials by Isomeric Effect," *ACS Applied Materials & Interfaces* 6, no. 14 (2014): 10870–10876, <https://doi.org/10.1021/am405470p>.
31. L. Sieuw, A. E. Lakraychi, D. Rambabu, et al., "Through-space Charge Modulation Overriding Substituent Effect: Rise of the Redox Potential at 3.35 V in a Lithium-Phenolate Stereoelectronic Isomer," *Chemistry of Materials* 32, no. 23 (2020): 9996–10006, <https://doi.org/10.1021/acs.chemmater.0c02989>.
32. L. Bernard, A. Jouhara, E. Quarez, et al., "Influence of Polymorphism on the Electrochemical Behavior of Dilithium (2, 3-Dilithium-oxy)-terephthalate vs. Li," *Inorganics* 10, no. 5 (2022): 62.
33. X. Guo, P. Apostol, X. Zhou, et al., "Towards the 4 V-Class n-Type Organic Lithium-Ion Positive Electrode Materials: The Case of Conjugated Triflimides and Cyanamides," *Energy & Environmental Science* 17, no. 1 (2024): 173–182, <https://doi.org/10.1039/D3EE02897F>.
34. Y. Zhang, P. Apostol, X. Guo, et al., "Validating the Reversible Redox of Alkali-Ion Disulfonyl-Methanide as Organic Positive Electrode Materials," *Materials Today Chemistry* 28 (2023): 101379, <https://doi.org/10.1016/j.mtchem.2023.101379>.
35. J. Wang, P. Apostol, D. Rambabu, et al., "Revealing the Reversible Solid-State Electrochemistry of Lithium-Containing Conjugated Oximates for Organic Batteries," *Science Advances* 9, no. 17 (2023): adg6079, <https://doi.org/10.1126/sciadv.adg6079>.
36. J. E. Bachman, L. A. Curtiss, and R. S. Assary, "Investigation of the Redox Chemistry of Anthraquinone Derivatives Using Density Functional Theory," *The Journal of Physical Chemistry A* 118, no. 38 (2014): 8852–8860, <https://doi.org/10.1021/jp5060777>.
37. C. Meng, N. An, S. Song, et al., "Accurate Prediction of Redox Potential and the Rational Design of Organic Molecular Electrode With Multi-Electron Active Centers for Supercapacitor," *Journal of Energy Storage* 102 (2024): 114122, <https://doi.org/10.1016/j.est.2024.114122>.
38. R. B. Araujo, A. Banerjee, P. Panigrahi, et al., "Designing Strategies to Tune Reduction Potential of Organic Molecules for Sustainable High Capacity Battery Application," *Journal of Materials Chemistry A* 5, no. 9 (2017): 4430–4454, <https://doi.org/10.1039/C6TA09760J>.
39. Z. Liu, X. Meng, F. Cui, and G. Zhu, "Designing Strategies for High-Redox-Potential Conjugated Carbonyl Organic Cathodes in Lithium-and Sodium-Ion Batteries," *Journal of Materials Chemistry A* 12, no. 35 (2024): 23769–23779, <https://doi.org/10.1039/D4TA03793F>.
40. Y. Liang, P. Zhang, S. Yang, Z. Tao, and J. Chen, "Fused Heteroaromatic Organic Compounds for High-Power Electrodes of Rechargeable Lithium Batteries," *Advanced Energy Materials* 3, no. 5 (2013): 600–605, <https://doi.org/10.1002/aenm.201200947>.
41. A. Shimizu, Y. Tsujii, H. Kuramoto, et al., "Nitrogen-Containing Polycyclic Quinones as Cathode Materials for Lithium-Ion Batteries With Increased Voltage," *Energy Technology* 2, no. 2 (2014): 155–158, <https://doi.org/10.1002/ente.201300148>.
42. F. Lambert, Y. Danten, C. Gatti, and C. Frayret, "A Tool for Deciphering the Redox Potential Ranking of Organic Compounds: A Case Study of Biomass-Extracted Quinones for Sustainable Energy," *Physical Chemistry Chemical Physics* 22, no. 36 (2020): 20212–20226, <https://doi.org/10.1039/D0CP02045A>.
43. D. Tomerini, C. Gatti, and C. Frayret, "Engineering of Unsubstituted Quinoid-Like Frameworks Enabling 2 V vs. Li+/Li Redox Voltage Tunability and Related Derivatives," *Physical Chemistry Chemical Physics* 17, no. 14 (2015): 8604–8608, <https://doi.org/10.1039/C4CP05998K>.
44. F. Lambert, Y. Danten, C. Gatti, B. Bocquet, A. A. Franco, and C. Frayret, "Carbonyl-Based Redox-Active Compounds as Organic Electrodes for Batteries: Escape From Middle–High Redox Potentials and Further Improvement?," *The Journal of Physical Chemistry A* 127, no. 24 (2023): 5104–5119, <https://doi.org/10.1021/acs.jpca.3c00478>.
45. C. Y. Go, J. Shin, M. K. Choi, I. H. Jung, and K. C. Kim, "Switchable Design of Redox-Enhanced Nonaromatic Quinones Enabled by Conjugation Recovery," *Advanced Materials* 36, no. 15 (2024): 2311155, <https://doi.org/10.1002/adma.202311155>.
46. M. Yao, S. Miyakawa, T. Kono, et al., "Phenazinetetrone Electrode for High-Energy-Density Organic Batteries via Oxygen- and Nitrogen-Based Redox Reactions," *Communications Materials* 6, no. 1 (2025): 287, <https://doi.org/10.1038/s43246-025-01016-6>.
47. M. Yao, N. Taguchi, H. Ando, N. Takeichi, and T. Kiyobayashi, "Improved Gravimetric Energy Density and Cycle Life in Organic Lithium-Ion Batteries With Naphthazarin-Based Electrode Materials," *Communications Materials* 1, no. 1 (2020): 70, <https://doi.org/10.1038/s43246-020-00071-5>.
48. A. E. Lakraychi, I. E. Udom, W. Ren, and Y. Yao, "Air-Stable High-Voltage Li-Ion Organic Cathode Enabled by Localized High-Concentration Electrolyte," *ChemSuschem* 18, no. 12 (2025): 202402779, <https://doi.org/10.1002/cssc.202402779>.
49. Z. Li, Q. Jia, Y. Chen, et al., "A Small Molecular Symmetric All-Organic Lithium-Ion Battery," *Angewandte Chemie International Edition* 61, no. 33 (2022): 202207221, <https://doi.org/10.1002/anie.202207221>.
50. L. Lin, Z. Lin, J. Zhu, et al., "A Semi-Conductive Organic Cathode Material Enabled by Extended Conjugation for Rechargeable Aqueous Zinc Batteries," *Energy & Environmental Science* 16, no. 1 (2023): 89–96, <https://doi.org/10.1039/D2EE02961H>.
51. T. Chen, H. Banda, J. Wang, J. J. Oppenheim, A. Franceschi, and M. Dincă, "A Layered Organic Cathode for High-Energy, Fast-Charging, and Long-Lasting Li-Ion Batteries," *ACS Central Science* 10 (2024): 569–578.

52. M. J. Frisch, G. W. Trucks, H. B. Schlegel, et al., "Gaussian 16, Revision C.01," (Gaussian Inc., 2016).
53. J.-D. Chai and M. Head-Gordon, "Long-Range Corrected Hybrid Density Functionals With Damped Atom-Atom Dispersion Corrections," *Physical Chemistry Chemical Physics* 10, no. 44 (2008): 6615–6620, <https://doi.org/10.1039/b810189b>.
54. V. A. Rassolov, J. A. Pople, M. A. Ratner, and T. L. Windus, "6-31G\* Basis Set for Atoms K Through Zn," *The Journal of Chemical Physics* 109, no. 4 (1998): 1223–1229, <https://doi.org/10.1063/1.476673>.
55. V. A. Rassolov, M. A. Ratner, J. A. Pople, P. C. Redfern, and L. A. Curtiss, "6-31G\* Basis Set for Third-Row Atoms," *Journal of Computational Chemistry* 22, no. 9 (2001): 976–984, <https://doi.org/10.1002/jcc.1058>.
56. V. Barone and M. Cossi, "Quantum Calculation of Molecular Energies and Energy Gradients in Solution by a Conductor Solvent Model," *The Journal of Physical Chemistry A* 102, no. 11 (1998): 1995–2001, <https://doi.org/10.1021/jp9716997>.
57. M. Cossi, N. Rega, G. Scalmani, and V. Barone, "Energies, Structures, and Electronic Properties of Molecules in Solution With the C-PCM Solvation Model," *Journal of Computational Chemistry* 24, no. 6 (2003): 669–681, <https://doi.org/10.1002/jcc.10189>.
58. J. Kruszewski and T. M. Krygowski, "Harmonic Oscillator Approach to the Definition of Aromaticity," *Bulletin of the Polish Academy of Sciences-Chemistry* 20, no. 9 (1972): 907–915.
59. J. Kruszewski and T. M. Krygowski, "Definition of Aromaticity Basing on the Harmonic Oscillator Model," *Tetrahedron Letters* 13, no. 36 (1972): 3839–3842, [https://doi.org/10.1016/S0040-4039\(01\)94175-9](https://doi.org/10.1016/S0040-4039(01)94175-9).
60. A. E. Lakrachi, F. Dolhem, F. Djedaïni-Pilard, A. Thiam, C. Frayret, and M. Becuwe, "Decreasing Redox Voltage of Terephthalate-Based Electrode Material for Li-Ion Battery Using Substituent Effect," *Journal of Power Sources* 359 (2017): 198–204, <https://doi.org/10.1016/j.jpowsour.2017.05.046>.
61. C. P. Frizzo and M. A. P. Martins, "Aromaticity in Heterocycles: New HOMA Index Parametrization," *Structural Chemistry* 23, no. 2 (2012): 375–380, <https://doi.org/10.1007/s11224-011-9883-z>.
62. T. Chen, H. Banda, L. Yang, et al., "High-Rate, High-Capacity Electrochemical Energy Storage in Hydrogen-Bonded Fused Aromatics," *Joule* 7, no. 5 (2023): 986–1002, <https://doi.org/10.1016/j.joule.2023.03.011>.
63. T. Ma, Q. Zhao, J. Wang, Z. Pan, and J. Chen, "A Sulfur Heterocyclic Quinone Cathode and a Multifunctional Binder for a High-Performance Rechargeable Lithium-Ion Battery," *Angewandte Chemie International Edition* 55, no. 22 (2016): 6428–6432, <https://doi.org/10.1002/anie.201601119>.
64. E. Hückel, "Quantentheoretische Beiträge zum Benzolproblem I. Die Elektronenkonfiguration des Benzols und Verwandter Verbindungen," *Zeitschrift fuer Physikalische Chemie* 70 (1931): 204–286, <https://doi.org/10.1007/BF01339530>.
65. X. Huang, X. Qiu, W. Wang, et al., "Activating Organic Electrode via Trace Dissolved Organic Molecules," *Journal of the American Chemical Society* 145, no. 47 (2023): 25604–25613, <https://doi.org/10.1021/jacs.3c06668>.
66. Y. Tateyama, A. Kagatsume, M. Yao, S. Matsuda, and K. Uosaki, "Exploration of Organic Cathode Active Materials With High Energy Densities for Li-Ion Batteries via First-Principles Calculations," *The Journal of Physical Chemistry C* 127, no. 27 (2023): 12867–12873, <https://doi.org/10.1021/acs.jpcc.3c02131>.
67. Y. Homma, H. Ogawa, and H. Matsui, "Exploring Organic Cathode Materials for Lithium-Ion Batteries Through Fragment Bonding and Discharge Simulation," *The Journal of Physical Chemistry C* 128, no. 6 (2024): 2304–2310, <https://doi.org/10.1021/acs.jpcc.3c06045>.
68. H. Kim, T. Goodson III, and P. M. Zimmerman, "Achieving Accurate Reduction Potential Predictions for Anthraquinones in Water and Aprotic Solvents: Effects of Inter- and Intramolecular H-Bonding and Ion Pairing," *The Journal of Physical Chemistry C* 120, no. 39 (2016): 22235–22247, <https://doi.org/10.1021/acs.jpcc.6b07558>.
69. A. MacColl, "Reduction Potentials of Conjugated Systems," *Nature* 163, no. 4135 (1949): 178.
70. D. D. Méndez-Hernández, P. Tarakeshwar, D. Gust, T. A. Moore, A. L. Moore, and V. Mujica, "Simple and Accurate Correlation of Experimental Redox Potentials and DFT-Calculated HOMO/LUMO Energies of Polycyclic Aromatic Hydrocarbons," *Journal of Molecular Modeling* 19, no. 7 (2013): 2845–2848, <https://doi.org/10.1007/s00894-012-1694-7>.
71. D. Wu, Z. Xie, Z. Zhou, P. Shen, and Z. Chen, "Designing High-Voltage Carbonyl-Containing Polycyclic Aromatic Hydrocarbon Cathode Materials for Li-Ion Batteries Guided by Clar's Theory," *Journal of Materials Chemistry A* 3, no. 37 (2015): 19137–19143, <https://doi.org/10.1039/C5TA05437K>.
72. E. Clar, *Polycyclic Hydrocarbons* (Springer-Verlag, 1964).
73. M. Randić, "Aromaticity of Polycyclic Conjugated Hydrocarbons," *Chemical Reviews* 103, no. 9 (2003): 3449–3606.
74. W. Gao and C. W. Coley, "The Synthesizability of Molecules Proposed by Generative Models," *Journal of Chemical Information and Modeling* 60, no. 12 (2020): 5714–5723, <https://doi.org/10.1021/acs.jcim.0c00174>.
75. J. Guo and P. Schwaller, "Directly Optimizing for Synthesizability in Generative Molecular Design Using Retrosynthesis Models," *Chemical Science* 16, no. 16 (2025): 6943–6956, <https://doi.org/10.1039/D5SC01476J>.
76. Q. Zhu and S. Hattori, "Organic Crystal Structure Prediction and Its Application to Materials Design," *Journal of Materials Research* 38, no. 1 (2023): 19–36, <https://doi.org/10.1557/s43578-022-00698-9>.
77. D. Zhou, I. Bier, B. Santra, et al., "A Robust Crystal Structure Prediction Method to Support Small Molecule Drug Development With Large Scale Validation and Blind Study," *Nature Communications* 16, no. 1 (2025): 2210, <https://doi.org/10.1038/s41467-025-57479-1>.

## Supporting Information

Additional supporting information can be found online in the Supporting Information section.

**Supporting File:** aenm71122-sup-0001-SuppMat.docx.